The Astrophysical Journal, 678:274–286, 2008 May 1

THE IMPORTANCE OF MAGNETIC-FIELD-ORIENTED THERMAL CONDUCTION IN THE INTERACTION OF SNR SHOCKS WITH INTERSTELLAR CLOUDS

S. Orlando[1] and F. Bocchino[1]
INAF-Osservatorio Astronomico di Palermo "G.S. Vaiana," Piazza del Parlamento 1, 90134 Palermo, Italy

and

F. Reale,[1,2] G. Peres,[1,2] and P. Pagano
Dipartimento di Scienze Fisiche ed Astronomiche, Università di Palermo, Piazza del Parlamento 1, 90134 Palermo, Italy
Received 2007 August 1; accepted 2008 January 9

ABSTRACT

We explore the importance of magnetic-field-oriented thermal conduction in the interaction of supernova remnant (SNR) shocks with radiative gas clouds and in determining the mass and energy exchange between the clouds and the hot surrounding medium. We perform 2.5-dimensional MHD simulations of a shock impacting on an isolated gas cloud, including anisotropic thermal conduction and radiative cooling; we consider the representative case of a Mach 50 shock impacting on a cloud 10 times denser than the ambient medium. We consider different configurations of the ambient magnetic field and compare MHD models with or without thermal conduction. The efficiency of thermal conduction in the presence of a magnetic field is, in general, reduced with respect to the unmagnetized case. The reduction factor strongly depends on the initial magnetic field orientation, and it is at a minimum when the magnetic field is initially aligned with the direction of the shock propagation. Thermal conduction contributes to the suppression of hydrodynamic instabilities, reducing the mass mixing of the cloud and preserving the cloud from complete fragmentation. Depending on the magnetic field orientation, the heat conduction may determine a significant energy exchange between the cloud and the hot surrounding medium which, while remaining always at levels less than those in the unmagnetized case, leads to a progressive heating and evaporation of the cloud. This additional heating may offset the radiative cooling of some parts of the cloud, preventing the onset of thermal instabilities.

Subject headings: conduction — ISM: clouds — ISM: magnetic fields — MHD — shock waves — supernova remnants

Online material: color figures

1. INTRODUCTION

The interaction of the shock waves of supernova remnants (SNRs) with the magnetized and inhomogeneous interstellar medium (ISM) is responsible for the great morphological complexity of SNRs and certainly plays a major role in determining the exchange of mass, momentum, and energy between diffuse hot plasma and dense clouds or clumps. These exchanges may, for example, occur through hydrodynamic ablation and thermal conduction, and, among other things, may lead to cloud crushing and the reduction of the Jeans mass, causing star formation.

The propagation of hot SNR shock fronts in the ISM and their interaction with local overdense gas clouds have been investigated with detailed hydrodynamic and MHD modeling. The most complete review of this problem in unmagnetized, nonconducting, and nonradiative limits is provided by Klein et al. (1994). These studies have shown that the cloud is disrupted by the action of both Kelvin-Helmholtz (KH) and Rayleigh-Taylor (RT) instabilities after several crushing times, with the cloud material expanding and diffusing into the ambient medium. An ambient magnetic field can both act as a confinement mechanism of the plasma and be modified by the interstellar flow and by local field stretching. Also, a strong magnetic field is known to limit hydrodynamic instabilities developing during the shock-cloud interaction by providing an additional tension at the interface between the cloud and the surrounding medium (e.g Mac Low et al. 1994; Jones et al. 1996).

The interaction of the shock with a *radiative* cloud has only recently been analyzed in detail (e.g., Mellema et al. 2002; Fragile et al. 2004). Two-dimensional calculations have shown that the effect of the radiative cooling is to break up the clouds into numerous dense and cold fragments that survive for many dynamical timescales. In the case of the interaction between magnetized shocks and radiative clouds, the magnetic field may enhance the efficiency of the radiative cooling, influencing the size and distribution of condensed cooled fragments (Fragile et al. 2005).

The role played by thermal conduction during the shock-cloud interaction has been less studied so far. In a previous paper, Orlando et al. (2005; hereafter Paper I) addressed this point in the unmagnetized limit. In particular, we have investigated the effect of thermal conduction and radiative cooling on cloud evolution and on the mass and energy exchange between the cloud and the surrounding medium; we have selected and explored two different physical regimes, chosen so that one or the other of the processes is dominant. In the case dominated by the radiative losses, we have found that the shocked cloud fragments into cold, dense, and compact filaments surrounded by a hot corona, which is ablated by thermal conduction. On the other hand, in the case dominated by thermal conduction, the shocked cloud evaporates in a few dynamical timescales. In both cases, we have found that thermal conduction is very effective in suppressing the hydrodynamic instabilities that would otherwise develop at the cloud boundaries, preserving the cloud from complete destruction. Orlando et al. (2006) and Miceli

[1] Consorzio COMETA, via Santa Sofia 64, 95123 Catania, Italy.
[2] INAF, Viale del Parco Mellini 84, 00136 Roma, Italy.

et al. (2006) have studied the observable effects of thermal conduction on the evolution of the shocked cloud in the X-ray band.

Here, we extend the previous studies by investigating the effect of thermal conduction in a magnetized medium, which has been unexplored so far. Of special interest to us is to investigate the role of anisotropic thermal conduction, which is funneled by locally organized magnetic fields, in the mass and energy exchange between ISM phases. In particular, we aim to address the following questions: How and under which physical conditions does the magnetic-field-oriented thermal conduction influence the evolution of the shocked cloud? How do the mass mixing of the cloud material and the energy exchange between the cloud and the surrounding medium depend on the orientation and strength of the magnetic field and on the efficiency of the thermal conduction?

To answer these questions, we take as a representative the model case of a shock with Mach number $\mathcal{M} = 50$ (corresponding to a postshock temperature $T \approx 4.7 \times 10^6$ K for an unperturbed medium with $T = 10^4$ K) impacting on an isolated cloud 10 times denser than the ambient medium. Paper I has shown that, in this case, thermal conduction dominates the evolution of the shocked cloud in the absence of a magnetic field. Around this basic configuration, we perform a set of MHD simulations, with different interstellar magnetic field orientations, and compare models calculated with thermal conduction turned either "on" or "off" in order to identify its effects on the cloud evolution.

The paper is organized as follows. In § 2 we describe the MHD model and the numerical setup, in § 3 we discuss the results, and finally in § 4 we draw our conclusions.

2. THE MODEL

We model the impact of a planar supernova shock front onto an isolated gas cloud. The shock propagates through a magnetized ambient medium, and the cloud is assumed to be small compared to the curvature radius of the shock.[3] The fluid is assumed to be fully ionized, with a ratio of specific heats $\gamma = 5/3$. The model includes radiative cooling, thermal conduction (including the effects of heat flux saturation), and resistivity effects. The shock-cloud interaction is modeled by numerically solving the time-dependent nonideal MHD equations (written in nondimensional conservative form):

$$\frac{\partial \rho}{\partial t} + \nabla \cdot (\rho \boldsymbol{u}) = 0, \tag{1}$$

$$\frac{\partial \rho \boldsymbol{u}}{\partial t} + \nabla \cdot (\rho \boldsymbol{u}\boldsymbol{u} - \boldsymbol{B}\boldsymbol{B}) + \nabla P_* = 0, \tag{2}$$

$$\frac{\partial \rho E}{\partial t} + \nabla \cdot [\boldsymbol{u}(\rho E + P_*) - \boldsymbol{B}(\boldsymbol{u} \cdot \boldsymbol{B})] = \nabla \cdot [\boldsymbol{B} \times (\eta \nabla \times \boldsymbol{B})] - \nabla \cdot \boldsymbol{F}_c - n_e n_{\rm H} \Lambda(T), \tag{3}$$

$$\frac{\partial \boldsymbol{B}}{\partial t} + \nabla \cdot (\boldsymbol{u}\boldsymbol{B} - \boldsymbol{B}\boldsymbol{u}) = -\nabla \times (\eta \nabla \times \boldsymbol{B}), \tag{4}$$

where

$$P_* = P + \frac{B^2}{2}, \quad E = \epsilon + \frac{1}{2}u^2 + \frac{1}{2}\frac{B^2}{\rho}$$

are the total pressure and the total gas energy (internal energy ϵ, kinetic energy, and magnetic energy), respectively, t is the time, $\rho = \mu m_{\rm H} n_{\rm H}$ is the mass density, $\mu = 1.26$ is the mean atomic mass (assuming cosmic abundances), $m_{\rm H}$ is the mass of the hydrogen atom, $n_{\rm H}$ is the hydrogen number density, $\boldsymbol{u}$ is the gas velocity, T is the temperature, $\boldsymbol{B}$ is the magnetic field, η is the resistivity according to Spitzer (1962), $\boldsymbol{F}_c$ is the conductive flux, and $\Lambda(T)$ represents the radiative losses per unit emission measure (e.g., Raymond & Smith 1977; Mewe et al. 1985; Kaastra & Mewe 2000). We use the ideal gas law, $P = (\gamma - 1)\rho\epsilon$.

In order to track the original cloud material, we use a tracer that is passively advected in the same manner as the density. We define $C_{\rm cl}$ as the mass fraction of the cloud inside the computational cell. The cloud material is initialized with $C_{\rm cl} = 1$, while $C_{\rm cl} = 0$ in the ambient medium.[4] During the shock-cloud evolution, the cloud and the ambient medium mix together, leading to regions with $0 < C_{\rm cl} < 1$. At any time t, the density of cloud material in a fluid cell is given by $\rho_{\rm cl} = \rho C_{\rm cl}$.

The thermal conductivity in an organized magnetic field is known to be highly anisotropic, and it can be extraordinarily reduced in the direction transverse to the field. The thermal flux, therefore, is locally split into two components, along and across the magnetic field lines, $\boldsymbol{F}_c = F_\parallel \boldsymbol{i} + F_\perp \boldsymbol{j}$, where

$$F_\parallel = \left[\frac{1}{(q_{\rm spi})_\parallel} + \frac{1}{(q_{\rm sat})_\parallel}\right]^{-1}, \quad F_\perp = \left[\frac{1}{(q_{\rm spi})_\perp} + \frac{1}{(q_{\rm sat})_\perp}\right]^{-1}, \tag{5}$$

to allow for a smooth transition between the classical and saturated conduction regime. In equation (5), $[q_{\rm spi}]_\parallel$ and $[q_{\rm spi}]_\perp$ represent the classical conductive flux along and across the magnetic field lines (Spitzer 1962):

$$(q_{\rm spi})_\parallel = -\kappa_\parallel (\nabla T)_\parallel \approx -5.6 \times 10^{-7} T^{5/2} (\nabla T)_\parallel$$

$$(q_{\rm spi})_\perp = -\kappa_\perp (\nabla T)_\perp \approx -3.3 \times 10^{-16} \frac{n_{\rm H}^2}{T^{1/2} B^2} (\nabla T)_\perp, \tag{6}$$

where $(\nabla T)_\parallel$ and $(\nabla T)_\perp$ are the thermal gradients along and across the magnetic field, and $\kappa_\parallel$ and $\kappa_\perp$ (in units of erg s^{-1} K^{-1} cm^{-1}) are the thermal conduction coefficients along and across the magnetic field lines,[5] respectively. The saturated flux along and across the magnetic field lines, $(q_{\rm sat})_\parallel$ and $(q_{\rm sat})_\perp$, are (Cowie & McKee 1977)

$$(q_{\rm sat})_\parallel = -{\rm sign}\left[(\nabla T)_\parallel\right] 5\phi\rho c_s^3,$$

$$(q_{\rm sat})_\perp = -{\rm sign}\left[(\nabla T)_\perp\right] 5\phi\rho c_s^3, \tag{7}$$

where c_s is the isothermal sound speed, and ϕ is a number of the order of unity; we set $\phi = 0.3$ according to the values suggested for a fully ionized cosmic gas: $0.24 < \phi < 0.35$ (Giuliani 1984; Borkowski et al. 1989; Fadeyev et al. 2002 and references therein). As discussed in Paper I, this choice implies that no thermal precursor develops during the shock propagation, which is consistent with the fact that no precursor is observed in young and middle-aged SNRs.

The initial unperturbed ambient medium is magnetized, isothermal (with temperature $T_{\rm ism} = 10^4$ K, corresponding to an isothermal sound speed $c_{\rm ism} = 11.5$ km s^{-1}), and uniform (with

[3] In the case of a small cloud, the SNR does not evolve significantly during the shock-cloud interaction, and the assumption of a planar shock is justified (see also Klein et al. 1994).

[4] We checked that the numerical scheme used ensures that $0 \le C_{\rm cl} \le 1$ is always true.

[5] For the values of T, $n_{\rm H}$, and B used here, $\kappa_\parallel/\kappa_\perp \approx 10^{16}$ at the beginning of the shock-cloud interaction.

TABLE 1
Summary of Initial Physical Parameters Characterizing the MHD Simulations

Simulation	Temperature (K)	Density (cm^{-3})	Velocity ($km\ s^{-1}$)
ISM	10^4	0.1	0.0
Cloud	10^3	1.0	0.0
Postshock medium	4.7×10^6	0.4	430

hydrogen number density $n_{\rm ism} = 0.1\ {\rm cm}^{-3}$; see Table 1). The gas cloud is in pressure equilibrium with its surrounding and has a circular cross section with radius $r_{\rm cl} = 1$ pc; its radial density distribution is given by

$$n_{\rm cl}(r) = n_{\rm ism} + \frac{n_{\rm cl0} - n_{\rm ism}}{\cosh[\sigma(r/r_{\rm cl})^{\sigma}]}, \quad (8)$$

where $n_{\rm cl0}$ is the hydrogen number density at the cloud center, r is the radial distance from the cloud center, and $\sigma = 10$. The above distribution describes a thin transition layer ($\sim 0.3 r_{\rm cl}$) around the cloud that smoothly brings the cloud density to the value of the surrounding medium.[6] The initial density contrast between the cloud center and the ambient medium is $\chi = n_{\rm cl0}/n_{\rm ism} = 10$. The cloud temperature is determined by the pressure balance across the cloud boundary.

The SNR shock front propagates with a velocity $w = \mathcal{M} c_{\rm ism}$ in the ambient medium, where $\mathcal{M}$ is the shock Mach number, and $c_{\rm ism}$ is the sound speed in the ISM; we consider a shock propagating with $\mathcal{M} = 50$, i.e., a shock velocity $w \approx 570\ {\rm km\ s}^{-1}$ and a temperature $T_{\rm psh} \approx 4.7 \times 10^6$ K. As discussed in Paper I, in this case (for a cloud with $r_{\rm cl} = 1$ pc and $\chi = 10$), the cloud dynamics would be dominated by thermal conduction in the absence of a magnetic field. The postshock conditions of the ambient medium well before the impact onto the cloud are given by the strong shock limit (Zel'dovich & Raizer 1966).

Starting from this basic configuration, we consider a set of simulations with different initial magnetic field orientations. We adopt a 2.5-dimensional (2.5D) Cartesian coordinate system (x, y), implying that the simulated clouds are cylinders extending infinitely along the z-axis perpendicular to the (x, y)-plane. The primary shock propagates along the y-axis. In this geometry, we consider three different field orientations: (1) parallel to the planar shock and perpendicular to the cylindrical cloud, (2) perpendicular to both the shock front and the cloud, and (3) parallel to both the shock and the cloud. The magnetic field components along the x- and the z-axes are enhanced by a factor $(\gamma + 1)/(\gamma - 1)$ (where γ is the ratio of specific heats) in the postshock region (in the strong shock limit; Zel'dovich & Raizer 1966), whereas the component along the y-axis is continuous across the shock. We include runs in the strong and weak magnetic field limits, considering initial field strengths of $|\boldsymbol{B}| = 2.63$, 1.31, 0.26, and 0 μG in the unperturbed ambient medium,[7] which correspond to $\beta_0 = 1$, 4, 100, and ∞, respectively, where $\beta_0 = P/(B^2/8\pi)$ is the ratio of thermal to magnetic pressure in the preshock region. This range of β_0 includes typical values inferred for the diffuse regions of the ISM (e.g., Mac Low & Klessen 2004) and for shock-cloud interaction regions in evolved SNR shells (e.g Bocchino et al. 2000). There is no magnetic field component exclusively associated with the cloud.

We follow the shock-cloud interaction for $3.5\tau_{\rm cc}$, where $\tau_{\rm cc} \approx \chi^{1/2} r_{\rm cl}/w$ is the cloud crushing time, i.e., the characteristic time of the shock transmission through the cloud; for the conditions considered here ($\chi = 10$ and $\mathcal{M} = 50$), $\tau_{\rm cc} \approx 5.4 \times 10^3$ yr. Each simulation is repeated either with or without thermal conduction for each field orientation. Table 2 lists the runs and the initial physical parameters of the simulations.

We numerically solve the set of MHD equations using FLASH (Fryxell et al. 2000), a multiphysics code that includes the PARAMESH library (MacNeice et al. 2000) for adaptive mesh refinement. The MHD equations are solved using the FLASH implementation of the Harten-Lax-van Leer-Einfeldt (HLLE) scheme (Einfeldt 1988). The code has been extended with additional computational modules to handle the radiative losses and anisotropic thermal conduction (see Pagano et al. 2007 for the details of the implementation).

The 2.5D Cartesian (x, y)-grid extends between -4 and 4 pc in the x-direction, and between -1.4 and 6.6 pc in the y-direction. Initially, the cloud is located at (x, y) = (0, 0), and the primary shock front propagates in the direction of the y-axis. At the coarsest resolution, the adaptive mesh algorithm used in the FLASH code uniformly covers the 2.5D computational domain with a mesh of 4^2 blocks, each with 8^2 cells. We allow for 5 levels of refinement, with resolution increasing twice at each refinement level. The refinement criterion adopted (Löhner 1987) follows changes in density and in temperature. This grid configuration yields an effective resolution of $\approx 7.6 \times 10^{-3}$ pc at the finest level, corresponding to $\approx$132 cells per cloud radius. In § 3.5, we discuss the effect of spatial resolution on our results, considering the additional runs TR-Bz4-hr and TR-Bz4-hr2, which use a setup identical to that used for run TR-Bz4, but with higher resolution ($\approx$264 and $\approx$528 cells per cloud radius, respectively; see Table 2).

We use a constant inflow boundary condition for the postshock gas at the lower boundary, with free outflow elsewhere. For runs with zero magnetic field ($\beta_0 = \infty$), we use reflecting boundary conditions at $x = 0$ along the symmetry axis of the problem and only evolve half of the grid.

3. RESULTS

3.1. *Dynamical Evolution*

Figures 1 and 2 show the evolution of the mass density in the (x, y)-plane in the simulations with $\beta_0 = \infty$ (runs NN and TR) and with $\beta_0 = 4$ (runs NN-Bx4, NN-By4, NN-Bz4, TR-Bx4, TR-By4, and TR-Bz4). The left and right halves of the panels show the result of models without and with thermal conduction and radiative losses, respectively.

From Figure 1, we note that thermal conduction drives the cloud evolution in the unmagnetized case ($\beta_0 = \infty$; run TR). After the initial compression due to the primary shock, the cloud expands and gradually evaporates due to heating driven by thermal conduction in a few dynamical timescales (Fig. 1, *right halves of panels*). The heat conduction strongly offsets the radiative cooling of some parts of the cloud, and no thermal or hydrodynamic instabilities (visible in run NN; see Fig. 1, *left halves of panels*) develop during the cloud evolution, making the cloud more stable and longer lived (the mass mixing is strongly reduced; see Paper I for more details).

We now discuss the effect of the magnetic-field-oriented (anisotropic) thermal conduction on the shock-cloud collision when an ambient magnetic field permeates the ISM. We first summarize the expected evolution in the presence of an ambient magnetic

[6] A finite transition layer, in general, is expected in real interstellar clouds due, for instance, to thermal conduction (Balbus 1986; see also Nakamura et al. 2006).

[7] The unmagnetized case (i.e., $|\boldsymbol{B}| = 0$) described here is analogous to the one studied in Paper I, except for the fact that in the present case the cloud is a cylinder rather than a sphere and has smooth boundaries.

TABLE 2
SUMMARY OF MHD SIMULATIONS

Run	$\lvert \boldsymbol{B} \rvert$ (μG)	β_0	Field Component	Thermal Conduction	Radiative Losses	Resolution[a]
NN	0	∞	...	no	no	132
NR	0	∞	...	no	yes	132
TN	0	∞	...	yes	no	132
TR	0	∞	...	yes	yes	132
NN-Bx4	1.31	4	B_x	no	no	132
NN-By4	1.31	4	B_y	no	no	132
NN-Bz4	1.31	4	B_z	no	no	132
TN-Bx4	1.31	4	B_x	yes	no	132
TN-By4	1.31	4	B_y	yes	no	132
TN-Bz4	1.31	4	B_z	yes	no	132
TR-Bx1	2.63	1	B_x	yes	yes	132
TR-By1	2.63	1	B_y	yes	yes	132
TR-Bz1	2.63	1	B_z	yes	yes	132
TR-Bx4	1.31	4	B_x	yes	yes	132
TR-By4	1.31	4	B_y	yes	yes	132
TR-Bz4	1.31	4	B_z	yes	yes	132
TR-Bx100	0.26	100	B_x	yes	yes	132
TR-By100	0.26	100	B_y	yes	yes	132
TR-Bz100	0.26	100	B_z	yes	yes	132
TR-Bz4-hr	1.31	4	B_z	yes	yes	264
TR-Bz4-hr2	1.31	4	B_z	yes	yes	528

NOTE.—In all runs, the shock Mach number is $\mathcal{M} = 50$, the density contrast is $\chi = 10$, and the cloud crushing time is $\tau_{cc} \approx 5.4 \times 10^3$ yr.
[a] Initial number of zones per cloud radius.

field, according to the well-established results of previous models without thermal conduction. We distinguish between fields perpendicular to the cylindrical clouds (i.e., with only B_x and B_y components, referred to as "external" fields by Fragile et al. 2005) and fields parallel to the cylindrical clouds (i.e., with only the B_z component, referred to as "internal" fields). In the former case, the magnetic field plays a dominant role along the cloud surface and in the wake of the cloud, where it reaches its highest strength (and where the plasma β reaches its lowest values; e.g., Mac Low et al. 1994; Jones et al. 1996). In the case of B_x, the magnetic field is trapped at the nose of the cloud, leading to a continuous increase of the magnetic pressure and field tension there (Fig. 2, *top*); in the case of B_y, the cloud expansion leads to an increase of magnetic pressure and field tension that is lateral to the cloud (Fig. 2, *middle*). In the case of B_z (internal field), the magnetic field, being parallel to the cylindrical cloud, modifies only the total effective pressure of the plasma (Jones et al. 1996); in the case of radiating shocks, the additional magnetic pressure may play a crucial role in the shocked cloud, preventing further compression of the cloud material (Fragile et al. 2005).

3.1.1. *External Magnetic Fields*

In the case of predominantly external magnetic fields, Mac Low et al. (1994) and Jones et al. (1996) have shown that hydrodynamic

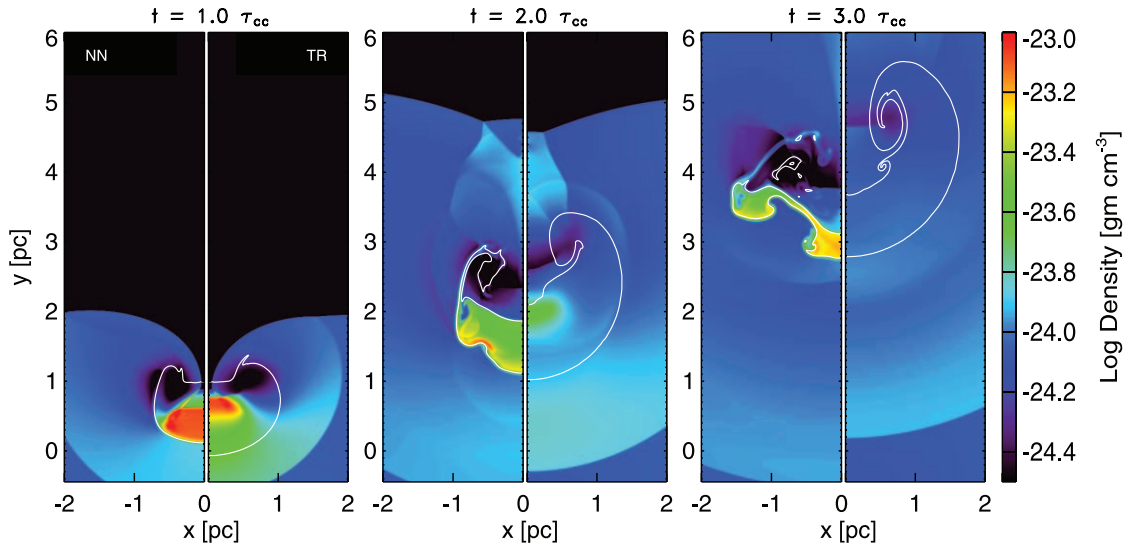

FIG. 1.—Mass density distribution (gm cm^{-3}) in the (x, y)-plane, in log scale, in the simulations NN (*left halves of panels*) and TR (*right halves of panels*), sampled at the labeled times in units of τ_{cc}. The contour encloses the cloud material.

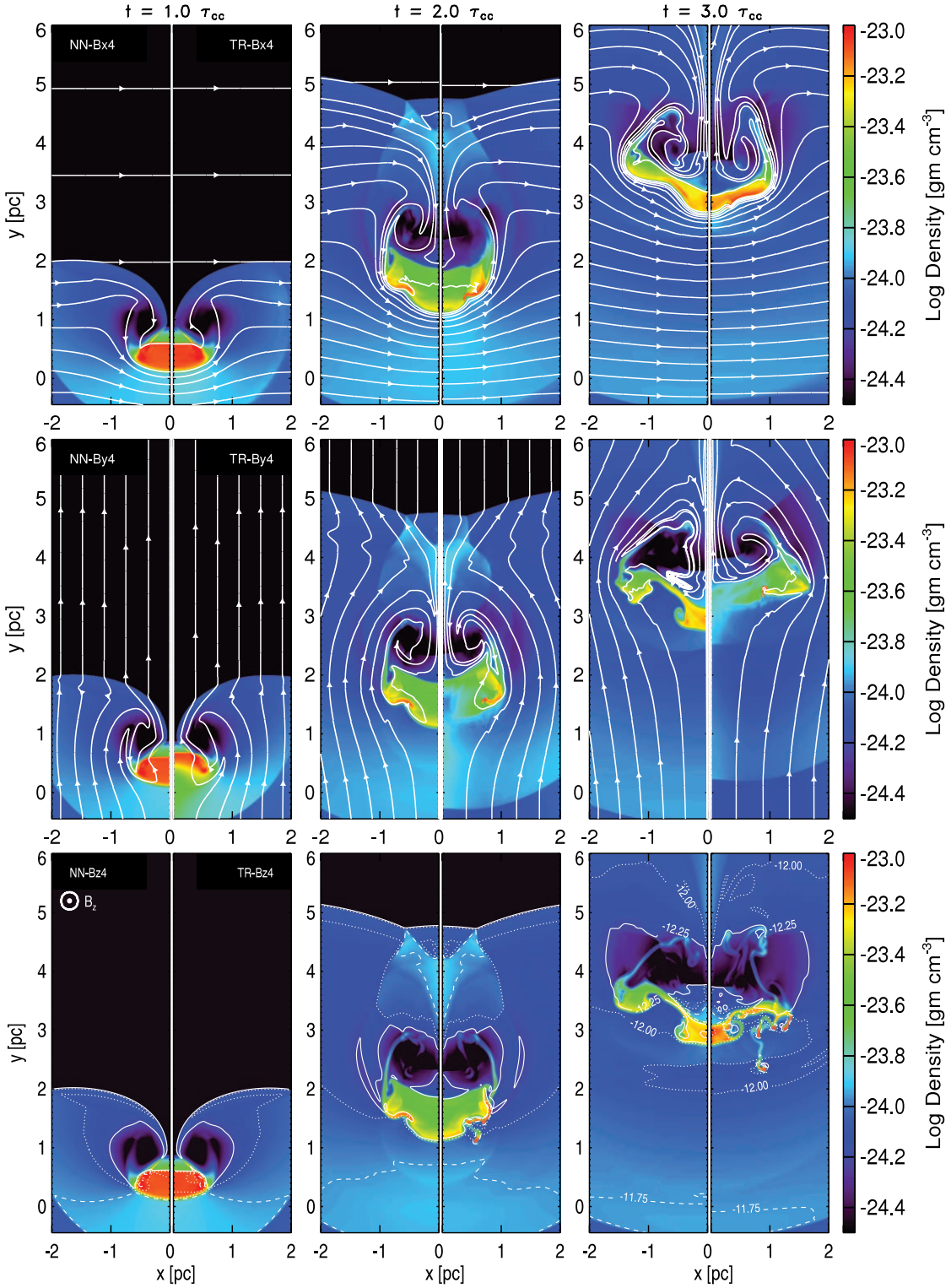

FIG. 2.— Same as Fig. 1, but for the simulations with $\beta_0 = 4$ and the magnetic field oriented along the *x*-axis (*top*), *y*-axis (*middle*), and *z*-axis (*bottom*). The figure shows the distribution in models either without (*left halves of panels*) or with (*right halves of panels*) thermal conduction and radiative losses. For runs NN-Bx4, TR-Bx4, NN-By4, and TR-By4, we plot the magnetic field lines; for runs NN-Bz4 and TR-Bz4, we include contours of $\log(B^2/8\pi)$.

instabilities can be suppressed even in models that neglect thermal conduction, due to the tension of the magnetic field lines, which maintain a more laminar flow around the cloud surface (see also Fragile et al. 2005). For a $\gamma = 5/3$ gas, the KH instabilities are suppressed if $\beta < 2/\mathcal{M}^2$, whereas RT instabilities are suppressed if $\beta < (2/\gamma)(\chi/\mathcal{M})^2$ (see also Chandrasekhar 1961). However, for the parameters used in this paper ($\chi = 10$ and $\mathcal{M} = 50$), the magnetic field cannot suppress KH instabilities in any of our runs, whereas the RT instabilities are suppressed only in runs that lead to a locally very strong field ($\beta < 0.05$). This can be seen in model NN-Bx4 (Fig. 2, *top*), which presents a large field increase at the cloud boundary compared to model NN (Fig. 1). In the latter case, the growth of KH and RT instabilities at the cloud boundary is much more evident than in NN-Bx4. On the other hand, hydrodynamic instabilities are suppressed more efficiently in models that include thermal conduction (runs TR-Bx4 and TR-By4), even

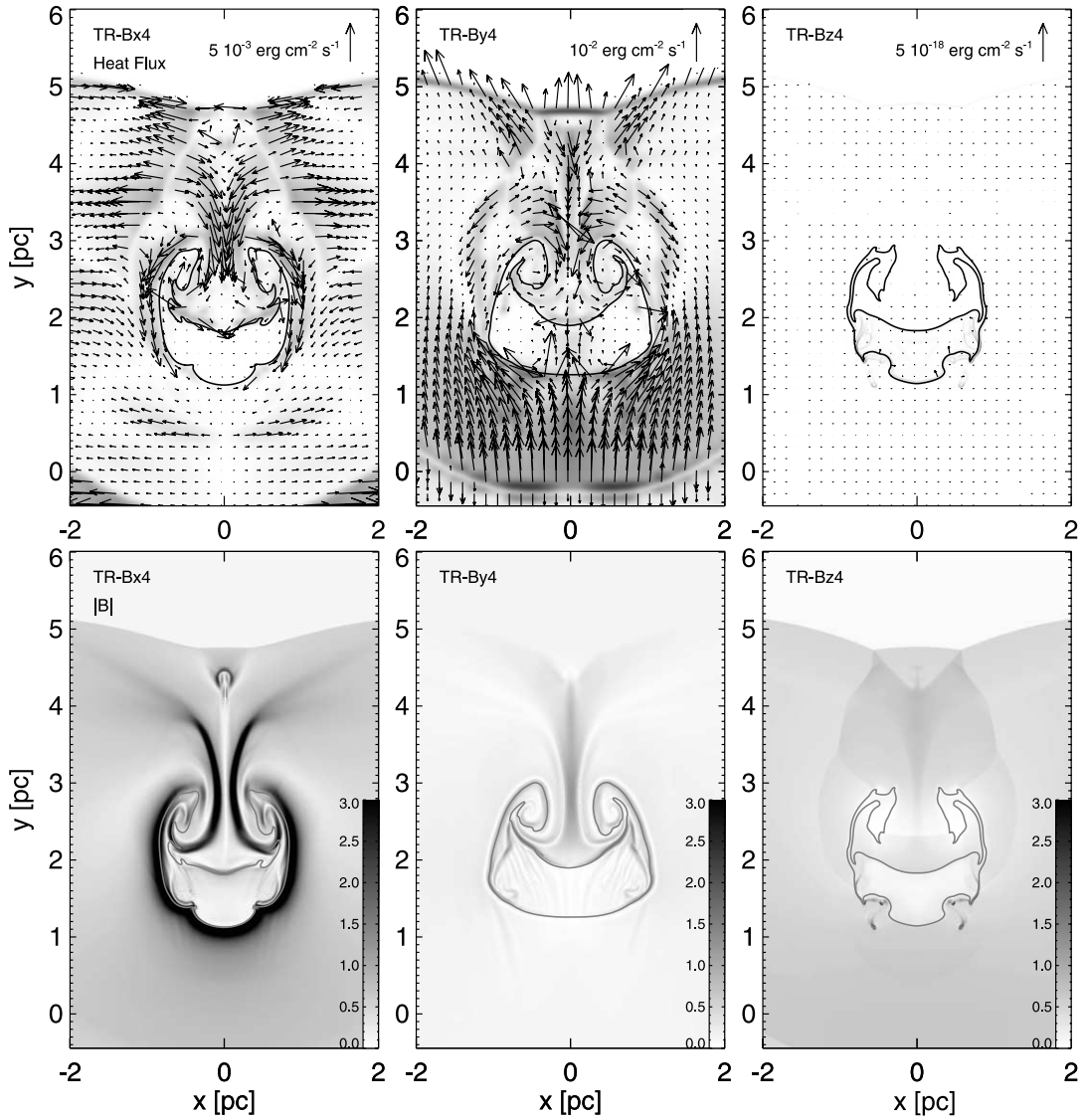

FIG. 3.—Heat flux (*top*) and magnetic field strength (*bottom*) distributions in the (*x, y*)-plane in the simulations TR-Bx4 (*left*), TR-By4 (*middle*), and TR-Bz4 (*right*), at time $t = 2\tau_{cc}$. The arrows in the upper panels linearly describe the heat flux and scale with respect to the reference value shown in the upper right corner of each panel. The scale of the magnetic field strength is linear and is given by the bar on the right, in units of 10 μG. The red contour encloses the cloud material. [*See the electronic edition of the Journal for a color version of this figure.*]

in cases with low field increase (for instance, in our B_y case), as can be seen in Figure 2 by comparing models NN-Bx4 and NN-By4 with models TR-Bx4 and TR-By4, respectively.

The thermal exchanges between the cloud and the surrounding medium strongly depend on the initial field orientation. Figure 3 shows the heat flux and magnetic field strength distributions in the (*x, y*)-plane in runs TR-Bx4, TR-By4, and TR-Bz4, at time $t = 2\tau_{cc}$. In our B_x case (Fig. 2, *top*), the magnetic field lines gradually envelop the cloud, reducing heat conduction through the cloud surface (Fig. 3, *left*); thermal exchanges between the cloud and the surrounding medium are channeled through small regions located to the side of the cloud. Cloud expansion and evaporation are strongly limited by the confining effect of the magnetic field (cf. the unmagnetized case TR in Fig. 1 with model TR-Bx4 in Fig. 2), which becomes up to 30 times stronger just outside the cloud than inside it (see also Fig. 3, *bottom left*). The consequent thermal insulation induces radiative cooling and condensation of the plasma into the cloud during the phase of cloud compression ($t < \tau_{cc}$). At the end of this phase, the cloud material has temperature $T \approx 10^5$ K and density $n_H \approx 10$ cm^{-3}, where primary and reverse shocks transmitted into the cloud are colliding; for these values of T and n_H, the Field length scale (Begelman & McKee 1990), derived from the ratio of the cooling timescale over the conduction timescale (see Paper I for details), is

$$l \approx 10^6 \frac{T^2}{n_H} \approx 3.2 \times 10^{-4} \text{ pc}. \quad (9)$$

The radiative cooling dominates over the effects of thermal conduction in cold and dense regions with dimensions larger than l. In contrast to our unmagnetized case TR, therefore, thermal instabilities develop in run TR-Bx4. One of these cold and dense structures is evident in Figure 2 (*top*) and is located at the cloud boundary near the nose of the cloud (at $x \approx 0.4$ pc and $y \approx 3.0$ pc) at $t = 3\tau_{cc}$.

In the B_y case, the initial field direction is mostly maintained in the cloud core during the evolution, allowing efficient thermal exchange between the core and the hot medium upwind of the cloud

(Fig. 3, *middle*); the core is gradually heated and evaporates in a few dynamical timescales. This is illustrated by run TR-By4 in Figure 2. On the other hand, the cloud is thermally insulated laterally where the magnetic field lines prevent thermal exchange between the cloud and the surrounding medium. Also, a strong magnetic field component along the *x*-axis develops in the wake of the cloud and inhibits thermal conduction with the medium downwind of the cloud. The thermal insulation to the side of the cloud determines the growth of thermal instabilities where shocks transmitted into the cloud collide (Fig. 2, *middle*).

In both external field configurations, elongated structures of strong field concentration are produced on the axis downwind of the cloud due to the focalization of the magnetized fluid flows there (Fig. 2, *top and middle*, and Fig. 3, *bottom*). These filamentary structures, identified as "flux ropes" by Mac Low et al. (1994), are formed by magnetic field lines stretched around the cloud shape and do not carry a significant amount of cloud material (as shown by the tracer $C_{\rm cl}$), although the plasma there moves with the cloud (see also Gregori et al. 2000).

3.1.2. *Internal Magnetic Fields*

Predominantly internal magnetic fields strongly suppress heat conduction, providing an efficient thermal insulation of the cloud material (Fig. 3, *right*). In a realistic configuration of an elongated cloud with finite length L along the z-axis, some heat would be conducted along the magnetic field lines. The characteristic timescales for the conduction along magnetic field lines is (see Paper I)

$$\tau_{\rm cond} \approx 2.6 \times 10^{-9} \frac{n_{\rm H} L^2}{T^{5/2}}. \quad (10)$$

We estimate that the cloud would thermalize in $\tau_{\rm cond} > 3.5\tau_{\rm cc}$ (i.e., the physical time covered by our simulations), if the length scale of the cloud along the z-axis were $L > 3$ pc. In this case, hydrodynamic instabilities would develop at the cloud boundary, as neither the magnetic field nor thermal conduction would be able to suppress them. The growth of these instabilities is clearly seen in Figure 2 (*bottom*). The combined effect of hydrodynamic instabilities and shocks transmitted into the cloud leads to unstable high-density regions at the cloud boundaries that trigger the development of thermal instabilities there (Fig. 2, *bottom*). However, as discussed by Fragile et al. (2005), internal magnetic field lines are expected to resist compression in the shocked cloud, thus reducing the cooling efficiency. In fact, in our run TR-Bz4, the cloud material is prevented from cooling below $T \approx 10^3$ K. Since thermal conduction does not play any significant role in the shock-cloud interaction, our B_z case leads to results similar to those obtained by Fragile et al. (2005), and we do not discuss this case further.

3.2. *Role of Thermal Conduction*

In this section, we study more quantitatively the effect of thermal conduction on cloud evolution and, in particular, on cloud compression and the magnetic field increase. To this end, we use the tracer defined in § 2 to identify zones whose content is made up of original cloud material by more than 90%. Then, we define the cross-sectional area of cloud material, $A_{\rm cl}(t)$, as the total area in the (x, y)-plane occupied by these zones. We define the cloud compression (or expansion) as $A_{\rm cl}/A_{\rm cl0}$, where $A_{\rm cl0}$ is the initial cross-sectional area. We also define an average mass-weighted temperature of the cloud and an average magnetic field strength associated with the cloud as

$$\langle T \rangle_{\rm cl} = \frac{\int_{A(C_{\rm cl}>0.9)} C_{\rm cl} \rho T \, da}{\int_{A(C_{\rm cl}>0.9)} C_{\rm cl} \rho \, da}, \quad (11)$$

$$\langle B \rangle_{\rm cl} = \frac{\int_{A(C_{\rm cl}>0.9)} C_{\rm cl} B \, da}{\int_{A(C_{\rm cl}>0.9)} C_{\rm cl} \, da}, \quad (12)$$

where we integrate on zones with $C_{\rm cl} > 0.9$. Note that our choice to consider cells with a passive tracer value of $C_{\rm cl} > 0.9$ is arbitrary. To determine how sensitive the results are to this value and, in particular, to small changes in it, we also derive our results considering the values $C_{\rm cl} > 0.85$ and $C_{\rm cl} > 0.95$. In all these cases, we find that the results derived with the different thresholds show the same trend, with differences of less than 10%.

Figure 4 shows the cloud compression, $A_{\rm cl}/A_{\rm cl0}$, the ratio of the average temperature of the cloud, $\langle T \rangle_{\rm cl}$, to the postshock temperature of the surrounding medium ($T_{\rm psh} = 4.7 \times 10^6$ K), and the ratio of the average magnetic field strength associated with the cloud, $\langle B \rangle_{\rm cl}$, to the initial field strength ($B_0 = 1.31$ μG, corresponding to $\beta_0 = 4$) as a function of time for models neglecting thermal conduction and radiation (hereafter NN* models), for models including conduction but neglecting radiation (TN* models), and for models including both conduction and radiation (TR* models); we also include the results derived from the unmagnetized case NR, with radiative cooling but without thermal conduction. The figure shows both the magnetized cases with $\beta_0 = 4$ and the unmagnetized cases (see Table 2).

In all the NN* models, either with (NN-Bx4, NN-By4, and NN-Bz4) or without (NN) the magnetic field, the evolution of the cloud compression and of the average cloud temperature is roughly the same (Fig. 4, *left*). The cloud is initially compressed over a timescale $t \approx \tau_{\rm cc}$ due to the ambient postshock pressure; during this phase, $\langle T \rangle_{\rm cl}$ rapidly increases. After $t \approx \tau_{\rm cc}$, the cloud partially re-expands, leading to a decrease of $\langle T \rangle_{\rm cl}$. In the last phase ($t > 2.0\tau_{\rm cc}$), the cloud is compressed again by the interaction with the "Mach stem" formed during the reflection of the primary shock at the symmetry axis, and $\langle T \rangle_{\rm cl}$ increases; later, $A_{\rm cl}/A_{\rm cl0}$ continues to decrease because of the mixing of the cloud material with the ambient medium (§ 3.3; see also Paper I), while $\langle T \rangle_{\rm cl}$ stabilizes at $\approx 0.17 T_{\rm psh}$.

The field increase in the cloud material depends on the initial configuration of $\boldsymbol{B}$ (Fig. 4, *bottom left*). In the case of external fields (B_x and B_y components), $\boldsymbol{B}$ is mainly intensified due to the stretching of field lines caused by sheared motion. In the B_x case, the magnetic field undergoes the greatest increase, and $\langle B \rangle_{\rm cl}$ keeps increasing during the whole evolution. In fact, the field is mainly intensified at the nose of the cloud, where the background flow continues to stretch the field lines during the evolution (Fig. 2, *top*). In the B_y case, the field increase occurs mainly to the side of the cloud, where the field lines are stretched along the cloud surface. In the case of internal fields (B_z component), the field increase is due to the squeezing of field lines through compression; $\langle B \rangle_{\rm cl}$ therefore follows the changes in $A_{\rm cl}/A_{\rm cl0}$, since the field is locked within the cloud material. Thus, the greatest field increase occurs at $t \approx \tau_{\rm cc}$, when the shocks transmitted into the cloud collide.

The effects of thermal conduction are greatest in the unmagnetized model (TN), which can be considered an extreme limiting case (Fig. 4, *left*). During the first stage of evolution ($t < 0.8\tau_{\rm cc}$), the cloud is heated efficiently by thermal conduction, and its average temperature increases rapidly to $\sim 0.5 T_{\rm psh}$. As a consequence,

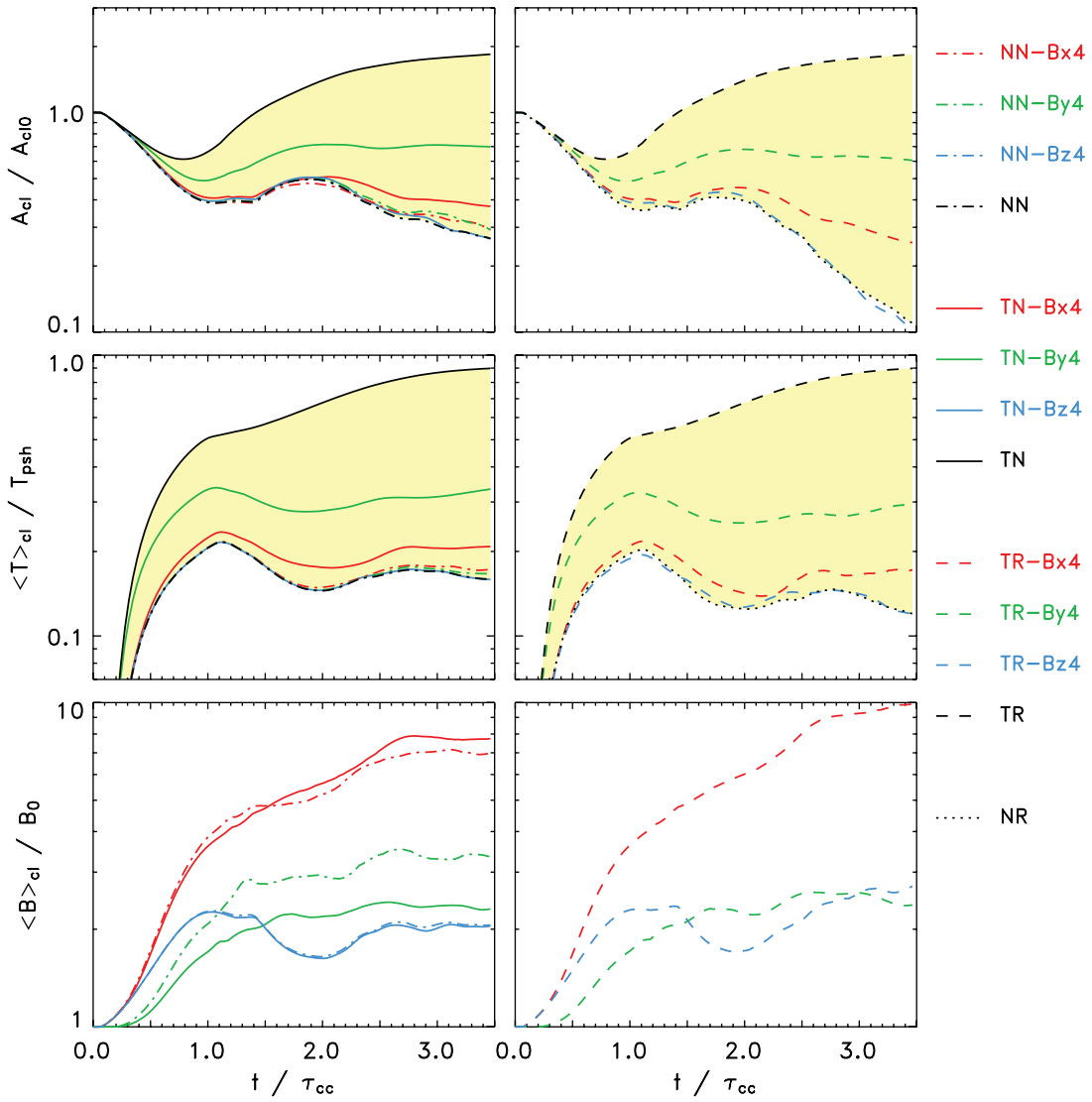

FIG. 4.—Evolution of cloud compression (*top*), of average temperature (*middle*), and of average magnetic field strength (*bottom*) of the cloud for runs that neglect thermal conduction and radiation (*dot-dashed lines; left*), for runs that include thermal conduction but neglect radiation (*solid lines; left*), for runs that include the radiation but neglect thermal conduction (*dotted lines; right*), and for runs that include both physical effects (*dashed lines; right*). The magnetized cases with $\beta_0 = 4$ are marked with red (initial magnetic field along the *x*-axis), green (initial $\boldsymbol{B}$ along the *y*-axis), and blue (initial $\boldsymbol{B}$ along the *z*-axis) lines; the unmagnetized cases are marked with black lines. The light yellow regions mark the locations of solutions that have thermodynamical characteristics in between the cases of maximum efficiency of thermal conduction (models TN and TR) and the cases without thermal conduction (models NN and NR). By comparing the positions of the curves of the magnetized models inside the yellow regions, it is possible to quantitatively assess the degree of suppression of the effects of thermal conduction by the magnetic fields.

the pressure inside the cloud increases, and the cloud re-expands earlier than in model NN. Afterward, the average cloud temperature, $\langle T \rangle_{\rm cl}$, keeps increasing up to $\sim 0.9 T_{\rm psh}$ at $t = 3.5\tau_{\rm cc}$.

In the case of predominantly external magnetic fields (models TN-Bx4 and TN-By4), thermal conduction still plays a significant role in cloud evolution, although its effects are not as large as in the unmagnetized case (TN). During the initial compression, thermal conduction contributes to cloud heating: the average temperature of the cloud reaches values larger than in models that neglect thermal conduction (compare TN* models with NN* models in the left panels of Fig. 4). This effect is greatest in the B_y case, which represents the configuration of field lines that allows the most efficient thermal exchange between the cloud and the hot environment (§ 3.1). At $t = 3.5\tau_{\rm cc}$, $\langle T \rangle_{\rm cl}$ in TN* models reaches values larger than in NN* models ($\approx 0.21 T_{\rm psh}$ in the B_x case and $\approx 0.33 T_{\rm psh}$ in the B_y case). For internal magnetic fields, thermal conduction plays no role in the evolution of the shocked cloud, being strongly ineffective due to $\boldsymbol{B}$ (§ 3.1). As a consequence, the TN-Bz4 model leads to the same results as the NN* models.

In general, therefore, the effects of thermal conduction in the presence of an ambient magnetic field are reduced with respect to the corresponding unmagnetized case, but are not entirely suppressed. This can be seen in Figure 4, where we have marked in light yellow the region between the fully conductive unmagnetized case (TN) and the case without thermal conduction (NN). The magnetized TN* models are always within this region, meaning that the effects of thermal conduction are never as large as in the unmagnetized case (TN), but are not completely suppressed, as in model NN.

We also note that thermal conduction indirectly influences the magnetic field increase. The main changes are in the B_y case and are due to the larger expansion of the cloud that reduces the increase of the field associated with the cloud, as the field is locked within the cloud material.

In our unmagnetized case TR (which includes thermal conduction and radiative cooling), thermal conduction prevents the onset of thermal instabilities, and the evolution of the shocked cloud is the same as that found in the TN model. In contrast to our unmagnetized case TR, Figure 4 shows that thermal instabilities develop in all our magnetized TR* runs, since the effects of thermal conduction are reduced by the magnetic field. The effects of radiative cooling are very strong for internal fields (our B_z case; see run TR-Bz4 in Fig. 4). In this case, heat conduction is totally suppressed by the magnetic field, and the evolutions of $A_{\rm cl}/A_{\rm cl0}$ and of $\langle T\rangle_{\rm cl}$ are the same as those found in the unmagnetized case with radiative cooling and without thermal conduction (model NR); at $t = 3.5\tau_{\rm cc}$, run TR-Bz4 (and NR) shows the largest cloud compression ($A_{\rm cl}/A_{\rm cl0} \approx 0.1$) and the lowest average cloud temperature ($\langle T\rangle_{\rm cl} \approx 0.12 T_{\rm psh}$). In the case of external fields (runs TR-Bx4 and TR-By4), the effects of heat conduction are reduced but not eliminated, and the results are intermediate between those derived for runs NR and TR (i.e., within the light yellow region in the right panels in Fig. 4). The cooling efficiency is largely reduced in our B_y case (run TR-By4), which has the magnetic field configuration that allows the most effective thermal conduction.

3.3. *Mass Mixing and Energy Exchange*

We use the tracer to derive the cloud mass, $M_{\rm cl}$, which we define as the total mass contained in zones whose content is made up of original cloud material by more than 90%:

$$M_{\rm cl} = L \int_{A(C_{\rm cl}>0.9)} C_{\rm cl}\rho\, da, \tag{13}$$

where L is the cloud length along the z-axis, and the integral is done on zones with $C_{\rm cl} > 0.9$. We investigate the mixing of cloud material with the ambient medium by defining the remaining cloud mass as $M_{\rm cl}/M_{\rm cl0}$, where $M_{\rm cl0}$ is the initial cloud mass.

The tracer also allows us to investigate the energy exchange between the cloud and the surrounding medium; we derive the internal energy, $\mathcal{I}_{\rm cl}$, and the kinetic energy, $\mathcal{K}_{\rm cl}$, of the cloud as

$$\mathcal{I}_{\rm cl} = L \int_{A(C_{\rm cl}>0.9)} C_{\rm cl}\rho\epsilon\, da, \tag{14}$$

$$\mathcal{K}_{\rm cl} = \frac{L}{2} \int_{A(C_{\rm cl}>0.9)} C_{\rm cl}\rho|\boldsymbol{u}|^2\, da, \tag{15}$$

where again L is the cloud length along the z-axis, and the integral is done on zones with $C_{\rm cl} > 0.9$. We also define the total energy of the cloud as

$$E_{\rm cl} = \mathcal{I}_{\rm cl} + \mathcal{K}_{\rm cl}. \tag{16}$$

Figure 5 shows the evolution of the cloud mass, $M_{\rm cl}/M_{\rm cl0}$, for NN*, TN*, and TR* models; again, we also include the unmagnetized case with radiative cooling and without thermal conduction (model NR). Both unmagnetized cases and magnetized cases with $\beta_0 = 4$ are shown. In models without thermal conduction and radiation (NN* models), the hydrodynamic instabilities drive the mass mixing of the cloud.[8] The mass-loss rate of the cloud, $\dot{m}_{\rm cl}$, increases significantly after $1.5\tau_{\rm cc}$ (i.e., after the hydrodynamic instabilities have fully developed at the cloud boundary), with $\dot{m}_{\rm cl} \approx 1.5\times10^{-6} L_{\rm pc}\, M_\odot\ {\rm yr}^{-1}$, where $L_{\rm pc}$ is the cloud length along the z-axis in units of pc; $\sim$20% of the cloud mass is contained in mixed zones at $t = 3.5\tau_{\rm cc}$. The only exception is run NN-Bx4 (with $\sim$15% of the cloud mass in mixed zones at $t = 3.5\tau_{\rm cc}$), since in this case, RT instabilities are partially suppressed by the magnetic field (compare run NN-Bx4 with runs NN-By4 and NN-Bz4 in Fig. 2).

In TN* models with external magnetic fields (TN-Bx4 and TN-By4), the mass-loss rate of the cloud is less efficient than in NN* models with $\dot{m}_{\rm cl} \approx 6\times10^{-7} L_{\rm pc}\, M_\odot\ {\rm yr}^{-1}$ (where $\sim$10% of the cloud mass is in mixed zones at $t = 3.5\tau_{\rm cc}$). In fact, in these cases, thermal conduction suppresses most of the hydrodynamic instabilities, and the mass loss mainly comes from cloud evaporation driven by thermal conduction rather than from hydrodynamic ablation. Note that our unmagnetized TN model is an extreme limit case in which the hydrodynamic instabilities are totally suppressed by thermal conduction, which drives the cloud mixing; in this case, the mass-loss rate is $\dot{m}_{\rm cl} \approx 1.5\times10^{-7} L_{\rm pc}\, M_\odot\ {\rm yr}^{-1}$ (where $\sim$5% of the cloud mass is in mixed zones at $t = 3.5\tau_{\rm cc}$).

In magnetized TR* models, the onset of thermal instabilities increases the mass-loss rate of the cloud with respect to the unmagnetized case ($\dot{m}_{\rm cl}$ ranges between $1.5\times10^{-6} L_{\rm pc}$ and $4\times10^{-6} L_{\rm pc}\, M_\odot\ {\rm yr}^{-1}$) due to the fragmentation of the cloud into dense and cold cloudlets. We expect, therefore, that the more cloud mass is mixed with the surrounding medium at the end of the evolution, the more limited will be the thermal exchange between the cloud and the hot ambient medium (and, therefore, the greater will be the efficiency of radiative cooling). In fact, the upper right panel of Figure 5 shows that mass mixing has the greatest efficiency in run TR-Bz4 (i.e., the case where thermal conduction is totally suppressed), which shows a mass-loss rate for the cloud similar to that derived from the unmagnetized NR model. On the other hand, in runs TR-Bx4 and TR-By4, the mass mixing is intermediate between those derived from runs NR and TR.

Figure 5 also shows the evolution of the ratios of the internal energy (*middle*) and the kinetic energy (*bottom*) of the cloud to the initial total energy of the cloud, $E_{\rm cl0}$. Among the magnetized cases considered, the greatest values of $\mathcal{I}_{\rm cl}$ are reached in our B_y case, which is the field configuration that allows the most efficient thermal exchange between the cloud and the environment; the increase of $\mathcal{I}_{\rm cl}$ is due to the heat conducted to the shocked cloud. Also, the B_y case leads to the greatest values of $\mathcal{K}_{\rm cl}$, because the cloud has a larger cross-sectional area (because of the larger cloud expansion due to the heating driven by heat conduction; see Fig. 4, *top*), and therefore offers a larger surface to the pressure of the shock front responsible for the cloud acceleration.

3.4. *Role of the Initial Field Strength*

In this section, we explore the effects of the initial field strength on the mass mixing and energy exchange of the cloud. Figure 6 shows the evolution of the cloud mass, $M_{\rm cl}/M_{\rm cl0}$ (*upper panel*), and of the total (internal plus kinetic) energy of the cloud, $E_{\rm cl}/E_{\rm cl0}$ (*lower panel*), for magnetized TR* models with different values of β_0. We discuss here only the cases of predominantly external magnetic fields (the B_x or B_y case), since no significant dependence on the initial field strength has been found in the case of predominantly internal magnetic fields (the B_z case).

Figure 6 shows that the initial field strength plays a significant role in the B_x case. In particular, models with greater values of β_0 show more efficient mixing of cloud material and a less rapid increase of the cloud energy. As discussed in § 3.3, in the B_x case, the rate of mass loss from the cloud is mainly driven by ablation through hydrodynamic instabilities (since thermal conduction is strongly suppressed by the magnetic field). On the other hand, in

[8] This is also true in our magnetized cases because, for the parameters used in this paper ($\mathcal{M} = 50$ and $\chi = 10$), the hydrodynamic instabilities are partially suppressed by the magnetic field only in runs evolving to strong fields (§ 3.1).

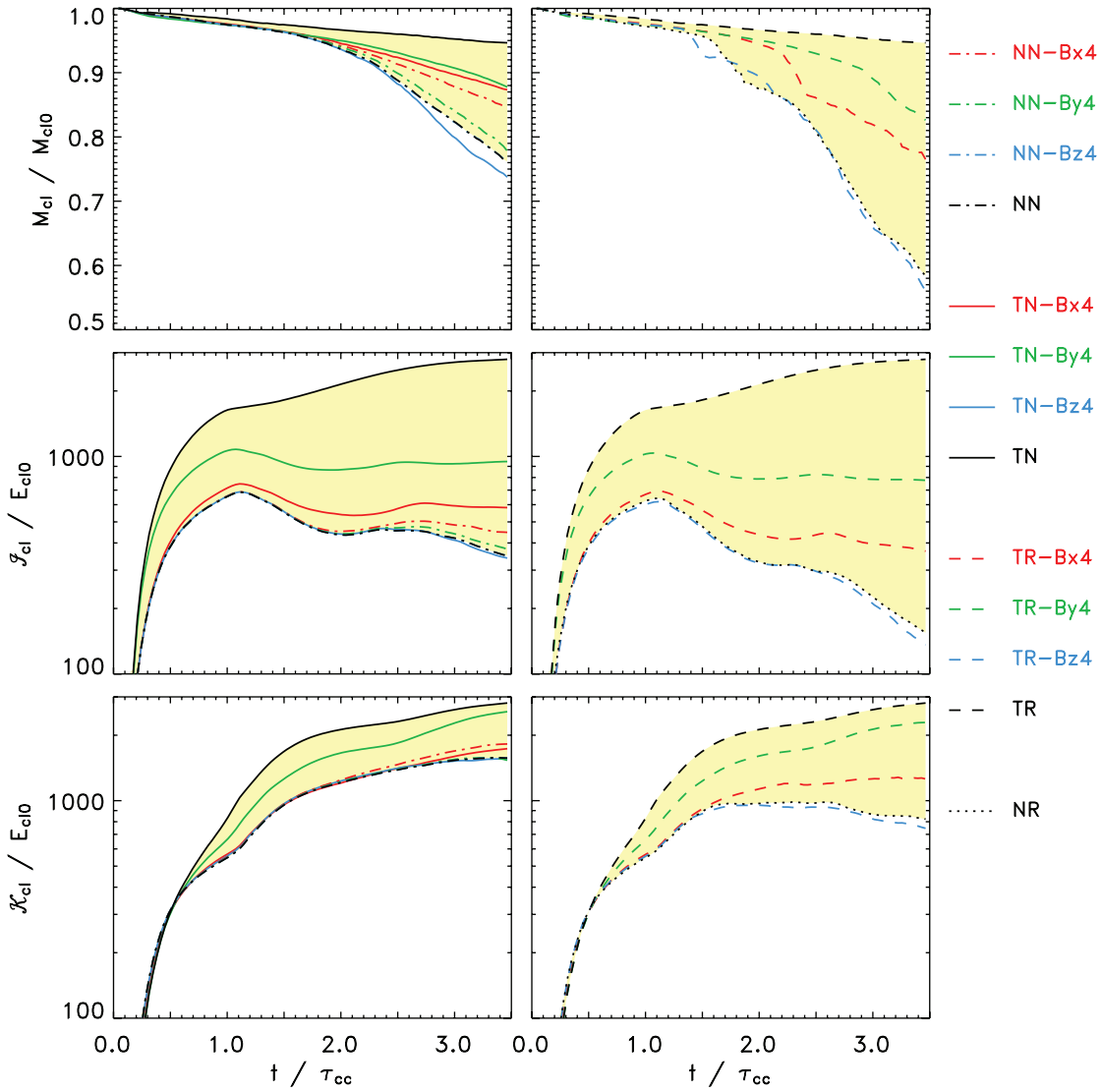

FIG. 5.—Same as Fig. 4, but for the evolution of the cloud mass (*top*), of the internal energy of the cloud (*middle*), and of the kinetic energy of the cloud (*bottom*).

the case of external fields, the instabilities can be dumped by the magnetic field, depending on its strength (§ 3.1.1). For instance, in the B_x case with $\beta_0 = 4$, we found that the RT instabilities are mostly suppressed by the magnetic field (Fig. 2, *top*). On the other hand, in the B_x case with $\beta_0 = 100$, the magnetic field is too weak to dump the hydrodynamic instabilities over the timescales considered; these instabilities, in turn, lead to the formation of regions dominated by radiative cooling, which triggers the development of thermal instabilities. Both the hydrodynamic and the thermal instabilities determine the cloud mass mixing (which is higher for higher values of β_0). In addition, the thermal instabilities reduce the increase of the cloud energy (which is less rapid for higher β_0) due to significant radiative losses.

In the B_y case, the initial field strength has a smaller influence on the dynamic and thermal evolution of the cloud than in the B_x case (see Fig. 6). In addition, in contrast to the B_x case, models with greater values of β_0 show less efficient mixing of cloud material and a more rapid increase of the cloud energy. In the B_y case, in fact, the hydrodynamic instabilities responsible for the mass mixing are mainly suppressed by thermal conduction rather than by the magnetic field, as in the B_x case. As a consequence, the higher the value of β_0, the more effective the thermal conduction in suppressing the instabilities and in heating the plasma, the less efficient the cloud mass mixing, and the more rapid the increase of the cloud energy.

3.5. *Effect of Spatial Resolution*

The effective resolution adopted in our simulations is ≈132 cells per cloud radius, a value above the resolution requirements suggested by Klein et al. (1994) for nonradiative clouds. However, for radiative clouds, we expect that the details of the plasma radiative cooling depend on the numerical resolution: a higher resolution may lead to different peak density and hence may influence the cooling efficiency of the gas, preventing further compression of the cloud. In the nonconducting regime, Fragile et al. (2005) found that the results generally converge for simulations with resolution larger than 100 cells per cloud radius (≲10% differences). In the simulations presented here, thermal conduction partially offsets radiative cooling in the case of external fields (B_x or B_y), alleviating the problem of numerical resolution (see also Paper I).

In order to check whether our adopted resolution is sufficient to capture the basic cloud evolution over the time interval considered, we compare three simulations (TR-Bz4, TR-Bz4-hr, and TR-Bz4-hr2) with different spatial resolutions (132, 264, and 528

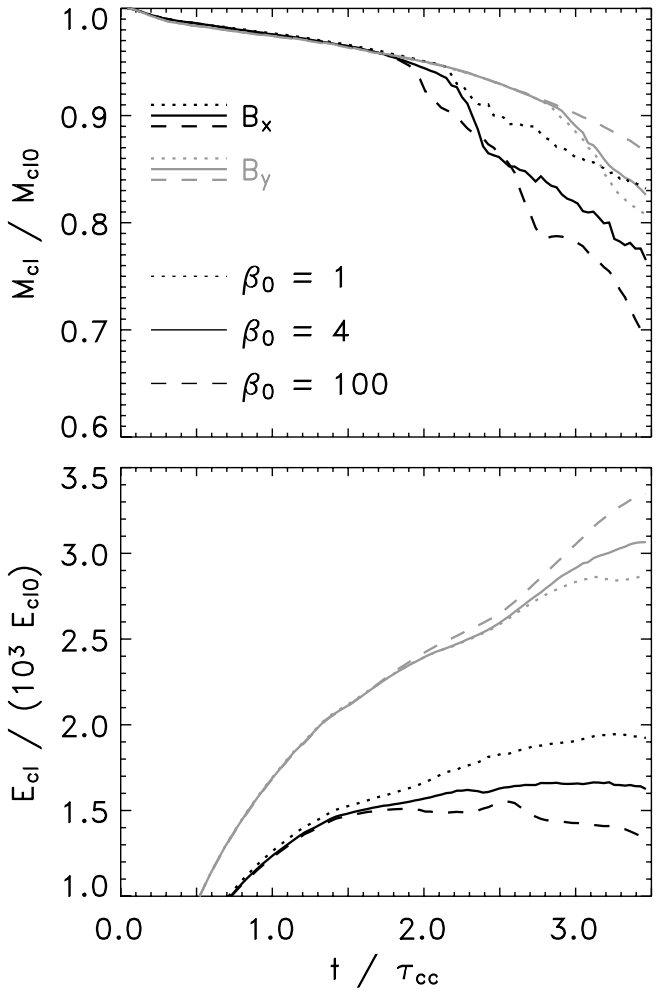

FIG. 6.—Evolution of the cloud mass (*top*) and of the total energy of the cloud (internal plus kinetic; *bottom*) for runs including both thermal conduction and radiative cooling (TR* models). The figure shows the simulations with the magnetic field oriented along the *x*-axis (*red lines*) or *y*-axis (*green lines*), and with $\beta_0 = 1$ (*dotted lines*), $\beta_0 = 4$ (*solid lines*), and $\beta_0 = 100$ (*dashed lines*). [*See the electronic edition of the Journal for a color version of this figure.*]

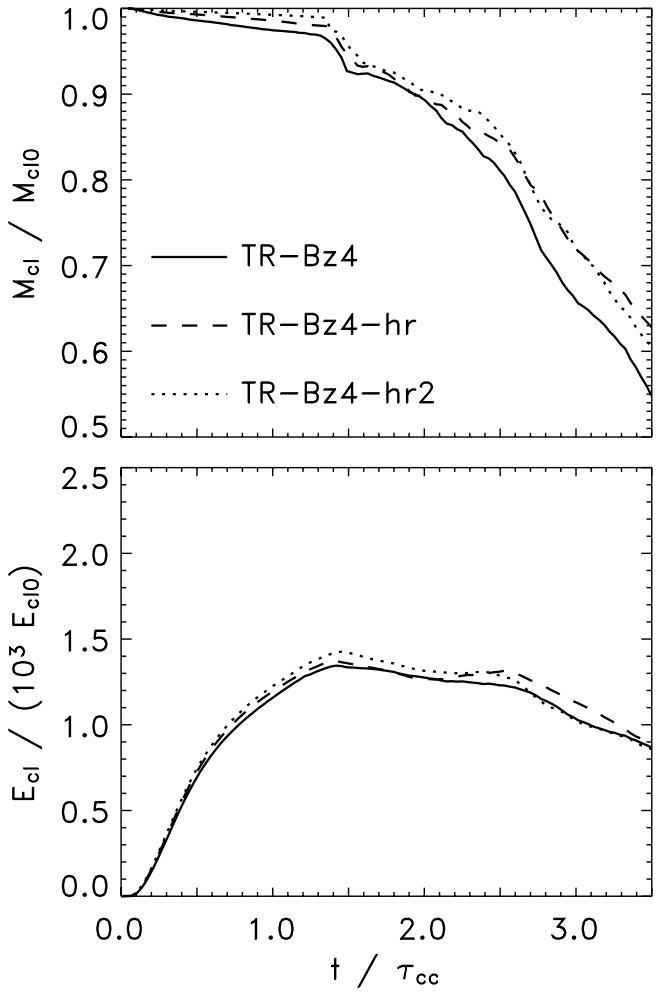

FIG. 7.—Same as Fig. 6, but for runs TR-Bz4 (*solid lines*), TR-Bz4-hr (*dashed lines*), and TR-Bz4-hr2 (*dotted lines*). [*See the electronic edition of the Journal for a color version of this figure.*]

zones per cloud radius, respectively) for the B_z case with $\beta = 4$, namely, one of the cases in which the growth of hydrodynamic and thermal instabilities is most prominent, and the effect of thermal conduction (which offsets the development of hydrodynamic and thermal instabilities) is negligible. Since this case is one of the most demanding for resolution, it can be considered a worst-case comparison of convergence.

Figure 7 compares the evolution of the cloud mass, M_{cl}/M_{cl0}, and of the total energy of the cloud, E_{cl}/E_{cl0}, for the three simulations, TR-Bz4, TR-Bz4-hr, and TR-Bz4-hr2. In general, we find that the results obtained with the three simulations agree quite well in their qualitative behavior, showing differences $\lesssim$10%. In runs TR-Bz4-hr and TR-Bz4-hr2, the remaining cloud mass and the total energy of the cloud are, in general, systematically higher than in run TR-Bz4. The larger mass mixing in TR-Bz4 is driven by the higher diffusion of the low-resolution grid down to very small structures, which tend to smear out concentrated density peaks, promoting mass mixing. The slightly lower energy of the cloud in TR-Bz4 is a consequence of the larger mass mixing derived in this run with respect to TR-Bz4-hr and TR-Bz4-hr2. Note that, in runs showing the onset of thermal instabilities (i.e NR* and TR* models), the sizes of the latter reach the resolution limit toward the end of the simulations, when the relevant physical processes are already at a late stage.

4. SUMMARY AND CONCLUSION

We have investigated the importance of magnetic-field-oriented thermal conduction in the interaction between an isolated elongated dense cloud and the interstellar shock wave of an evolved SNR shell through numerical MHD simulations. To our knowledge, these simulations represent the first attempt to model the shock-cloud interaction that simultaneously considers magnetic fields, radiative cooling, and anisotropic thermal conduction. Our findings lead to several conclusions:

1. In general, we found that the effects of thermal conduction on the evolution of the shocked cloud are reduced in the presence of an ambient magnetic field with respect to the unmagnetized cases investigated in Paper I. The efficiency of anisotropic thermal conduction strongly depends on the initial magnetic field orientation and configuration. This efficiency is greatest when the initial $\boldsymbol{B}$ is aligned with the direction of propagation of the shock front, and is smallest when $\boldsymbol{B}$ is aligned with the cylindrical cloud, namely when heat conduction is completely suppressed by the magnetic field.

2. We found that hydrodynamic instabilities are efficiently suppressed by anisotropic thermal conduction when the initial magnetic

field is perpendicular to the cylindrical cloud (a configuration referred to as "external fields"). On the other hand, in the case where $\boldsymbol{B}$ is parallel to the cylindrical axis of the cloud (i.e., when the field only has a component along the z-axis), hydrodynamic instabilities develop at the cloud boundary. We found that, for the parameters of the simulations chosen, the magnetic tension alone is unable to suppress hydrodynamic instabilities.

3. As for thermal instabilities, we found that, depending on the orientation of the magnetic field, the heat flux contributes to the heating of some parts of the cloud, reducing the efficiency of radiative cooling there, and preventing any thermal instability.

4. The mass loss of the cloud due to mixing with the surrounding medium is mainly driven by hydrodynamic instabilities; in the case of external fields (where initial $\boldsymbol{B}$ is perpendicular to the cylindrical cloud), anisotropic thermal conduction reduces the mass mixing of the cloud. In any of our cases, the mass-loss rate is larger than that in the corresponding unmagnetized case ($\dot{m}_{\rm cl} \approx 1.5 \times 10^{-7} L_{\rm pc}\, M_\odot\ {\rm yr}^{-1}$; i.e., $\sim$5% of the cloud mass is in mixed zones at $t = 3.5\tau_{\rm cc}$), but can get very high when thermal conduction is completely suppressed ($\dot{m}_{\rm cl} \approx 4 \times 10^{-6} L_{\rm pc}\, M_\odot\ {\rm yr}^{-1}$; i.e., $\sim$45% of the cloud mass is in mixed zones at $t = 3.5\tau_{\rm cc}$).

5. Thermal conduction mostly rules the energy exchange between the cloud and surrounding medium. The exchange is favored when the magnetic field configuration is such that the conductive flow is not suppressed (i.e., the external field configurations, the B_x and B_y cases), but it is never as high as in the absence of a magnetic field. In the B_y case, the cloud core is efficiently heated and evaporates in few dynamical timescales.

6. In general, the initial magnetic field strength has a small influence on the dynamic and thermal evolution of the shocked cloud for the ranges of values explored in this paper (namely $0.26\ \mu{\rm G} \leq |\boldsymbol{B}| \leq 2.63\ \mu{\rm G}$).

It is worth noting that some details of our simulations depend on the choice of the model parameters. For instance, the onset of thermal instabilities or the evaporation of the whole cloud depends on the initial shock Mach number and on the density and dimensions of the cloud. The cases that we present here (i.e., $\mathcal{M} = 50$, $\chi = 10$, and different configurations of $\boldsymbol{B}$) are representative of a regime in which both thermal conduction and radiative cooling play important roles in the evolution of the shocked cloud. Nevertheless, our analysis proves that anisotropic thermal conduction cannot be neglected in investigations of the evolution of shocked interstellar clouds.

In our simulations, we consider laminar thermal conduction, although regions of strong turbulence of different strengths and extents develop in the system (for instance, at the shear layers along the cloud boundary or at the vortex sheets in the cloud wake). In fact, the turbulence in these regions may have a significant effect on thermal conduction, and lead to significant deviations of thermal conductivity from its laminar values (e.g., Narayan & Medvedev 2001; Lazarian 2006); in some cases, the turbulence may enhance the heat transfer, exceeding the classical Spitzer value (Lazarian 2006). As a result, thermal conduction may not only be anisotropic (in the presence of the magnetic field) but also "inhomogeneous" due to the presence of turbulence. However, even modeling accurately the turbulent thermal conductivity, we do not expect significant changes in the results of our B_z case, as thermal conduction is strongly ineffective in the whole spatial domain; in the remaining cases (B_x and B_y), our modeled thermal conductivity could be underestimated in regions of strong turbulence, affecting some details of the simulations but not the main conclusion of the paper that, in general, anisotropic thermal conduction can play an important role in the evolution of the shocked cloud.

Note also that the field configurations studied in this work are highly idealized. More realistic fields are expected to have more complex topologies, and the field can often be tangled and chaotic. In the latter case, thermal conduction will approach isotropy, whereas the effect of MHD turbulence is expected to partially suppress the heat transfer within a factor of $\sim$5 below the classical Spitzer estimate[9] (Narayan & Medvedev 2001; Lazarian 2006). The shock-cloud collision in the presence of an organized ambient magnetic field, discussed here, and that in the absence of a magnetic field can be considered as extreme cases: the former leads to highly anisotropic thermal conduction, the latter to the classical Spitzer thermal conduction. The case of a chaotic magnetic field is expected to fall in between these two.

Our simulations were carried out in 2.5D Cartesian geometry, implying that the modeled clouds are elongated along the z-axis. This choice is expected to affect some details of the simulations but not our main conclusions. If one were to adopt a 3D Cartesian geometry and model a spherical cloud, a highly symmetric shock transmitted into that cloud that converges on the symmetry axis would lead to compression stronger than those found in our 2.5D simulations, enhancing the radiative cooling. Also, 3D simulations would provide an additional degree of freedom for hydrodynamic instabilities, increasing the mass-loss rate of the cloud in the cases in which the mass mixing of cloud material is driven by instabilities. Note that, for a spherical cloud, our B_x and B_z cases no longer differ.

Finally, we assume in our simulations that the cloud and the ambient material have the same composition, implying that microscopic mass mixing due to shear instabilities is irrelevant. Under more realistic conditions, a cold dense cloud might have a different composition from the hot ambient flow, and the degree of microscopic mixing might translate into different spectral signatures of the system. In this case, species diffusion could also be important, along with thermal conduction, to determine the degree of microscopic mixing of the materials; consequently, one would have to ask about the typical values of the Lewis number (i.e., the ratio of thermal diffusivity to mass diffusivity) in the system.

It is worth emphasizing that the quantitative results of our simulations depend on the physical parameters of the model (shock Mach number, density contrast, the dimension of the cloud, etc.), as well as on the basic assumptions of the model (geometry of the cloud, geometry of the ambient magnetic field, laminar thermal conduction, composition of the cloud and of the ambient medium, etc.). Nevertheless, our results undoubtedly show that magnetic-field-oriented thermal conduction can play an important role in the evolution of the shock-cloud interaction (which depends on the magnetic field orientation and configuration) and, in particular, in the mass and energy exchange between the cloud and the hot surrounding medium. We conclude, therefore, that a self-consistent and quantitative description of the interaction between magnetized shock waves and interstellar gas clouds should include the effects of thermal conduction.

The results presented here are interesting for the study of middle-aged SNR shells expanding into a magnetized ISM and whose morphology is affected by ISM inhomogeneities (for instance, G272.2-3.2 [e.g., Egger et al. 1996], the Cygnus Loop [e.g., Patnaude et al. 2002], and the Vela SNR [e.g., Miceli et al. 2005]). It will be interesting to extend the present study by modeling the shock-cloud interaction in 3D with radiative cooling, anisotropic thermal conduction, and magnetic field, and to consider detailed comparisons of model results with observations.

[9] As already discussed, the MHD turbulence can even enhance the heat transfer in some cases (Lazarian 2006).

The authors thank Timur Linde for his help with the MHD portion of FLASH and the referee for constructive and helpful criticism. The software used in this work was in part developed by the DOE-supported ASC/Alliance Center for Astrophysical Thermonuclear Flashes at the University of Chicago, using modules for thermal conduction and optically thin radiation built at the Osservatorio Astronomico di Palermo. Most of the simulations were executed at CINECA (Bologna, Italy) in the framework of the INAF-CINECA agreement on "High Performance Computing Resources for Astronomy and Astrophysics." This work makes use of results produced by the PI2S2 Project managed by the Consorzio COMETA, a project cofunded by the Italian Ministry of University and Research (MIUR) within the Piano Operativo Nazionale "Ricerca Scientifica, Sviluppo Tecnologico, Alta Formazione" (PON 2000–2006); more information is available at http://www.pi2s2.it and http://www.consorziocometa.it. This work was supported in part by Istituto Nazionale di Astrofisica.

REFERENCES

Balbus, S. A. 1986, ApJ, 304, 787
Begelman, M. C., & McKee, C. F. 1990, ApJ, 358, 375
Bocchino, F., Maggio, A., Sciortino, S., & Raymond, J. 2000, A&A, 359, 316
Borkowski, K. J., Shull, J. M., & McKee, C. F. 1989, ApJ, 336, 979
Chandrasekhar, S. 1961, Hydrodynamic and Hydromagnetic Stability (Oxford: Clarendon)
Cowie, L. L., & McKee, C. F. 1977, ApJ, 211, 135
Egger, R., Greiner, J., & Aschenbach, B. 1996, in Roentgenstrahlung from the Universe, ed. H. U. Zimmermann, J. E. Trümper, & H. Yorke (MPE Rep. 263; Garching: MPE), 247
Einfeldt, B. 1988, SIAM J. Numer. Anal., 25, 357
Fadeyev, Y. A., Le Coroller, H., & Gillet, D. 2002, A&A, 392, 735
Fragile, P. C., Anninos, P., Gustafson, K., & Murray, S. D. 2005, ApJ, 619, 327
Fragile, P. C., Murray, S. D., Anninos, P., & van Breugel, W. 2004, ApJ, 604, 74
Fryxell, B., et al. 2000, ApJS, 131, 273
Giuliani, J. L. 1984, ApJ, 277, 605
Gregori, G., Miniati, F., Ryu, D., & Jones, T. W. 2000, ApJ, 543, 775
Jones, T. W., Ryu, D., & Tregillis, I. L. 1996, ApJ, 473, 365
Kaastra, J. S., & Mewe, R. 2000, in Atomic Data Needs for X-ray Astronomy, ed. M. A. Bautista, T. R. Kallman, & A. K. Pradhan (Washington: NASA), 161
Klein, R. I., McKee, C. F., & Colella, P. 1994, ApJ, 420, 213
Lazarian, A. 2006, ApJ, 645, L25
Löhner, R. 1987, Comput. Methods Appl. Mech. Eng., 61, 323
Mac Low, M., & Klessen, R. S. 2004, Rev. Mod. Phys., 76, 125
Mac Low, M., McKee, C. F., Klein, R. I., Stone, J. M., & Norman, M. L. 1994, ApJ, 433, 757
MacNeice, P., Olson, K. M., Mobarry, C., de Fainchtein, R., & Packer, C. 2000, Comput. Phys. Comm., 126, 330
Mellema, G., Kurk, J. D., & Röttgering, H. J. A. 2002, A&A, 395, L13
Mewe, R., Gronenschild, E. H. B. M., & van den Oord, G. H. J. 1985, A&AS, 62, 197
Miceli, M., Bocchino, F., Maggio, A., & Reale, F. 2005, A&A, 442, 513
Miceli, M., Reale, F., Orlando, S., & Bocchino, F. 2006, A&A, 458, 213
Nakamura, F., McKee, C. F., Klein, R. I., & Fisher, R. T. 2006, ApJS, 164, 477
Narayan, R., & Medvedev, M. V. 2001, ApJ, 562, L129
Orlando, S., Bocchino, F., Peres, G., Reale, F., Plewa, T., & Rosner, R. 2006, A&A, 457, 545
Orlando, S., Peres, G., Reale, F., Bocchino, F., Rosner, R., Plewa, T., & Siegel, A. 2005, A&A, 444, 505 (Paper I)
Pagano, P., Reale, F., Orlando, S., & Peres, G. 2007, A&A, 464, 753
Patnaude, D. J., Fesen, R. A., Raymond, J. C., Levenson, N. A., Graham, J. R., & Wallace, D. J. 2002, AJ, 124, 2118
Raymond, J. C., & Smith, B. W. 1977, ApJS, 35, 419
Spitzer, L. 1962, Physics of Fully Ionized Gases (2nd ed.; New York: Interscience)
Zeldovich, Y. B., & Raizer, Y. P. 1966–1967, Physics of Shock Waves and High-Temperature Hydrodynamic Phenomena (New York: Academic Press)